Environmental Research 204 (2022) 112126

Contents lists available at ScienceDirect

Environmental Research

journal homepage: www.elsevier.com/locate/envres

Electrocatalytic activity of calcined manganese ferrite solid nanospheres in the oxygen reduction reaction

J.X. Flores-Lasluisa [a], D. Salinas-Torres [a,*], M.V. López-Ramón [b,**], C. Moreno-Castilla [c,***], M. A. Álvarez [b], E. Morallón [a], D. Cazorla-Amorós [d]

[a] Departamento de Química Física e Instituto Universitario de Materiales, Universidad de Alicante, Ap. 99, E-03080, Alicante, Spain
[b] Departamento de Química Inorgánica y Orgánica, Facultad de Ciencias Experimentales, Universidad de Jaén, E-23071, Jaén, Spain
[c] Departamento de Química Inorgánica, Facultad de Ciencias, Universidad de Granada, E-18071, Granada, Spain
[d] Departamento de Química Inorgánica e Instituto Universitario de Materiales, Universidad de Alicante, Ap. 99, E-03080, Alicante, Spain

ARTICLE INFO

Keywords:
Manganese ferrite
Manganese oxidation states
Carbon black
Electrocatalyst
Oxygen reduction reaction

ABSTRACT

In this study, we synthesized $MnFe_2O_4$ solid nanospheres (MSN) calcined at different temperatures (200–500 °C) and MSN-based materials mixed with carbon black, for their use as electrocatalysts in the oxygen reduction reaction (ORR) in alkaline medium (0.1 M KOH). It was demonstrated that the calcination temperature of MSN material determined its chemical surface composition and microstructure and it had an important effect on the electrocatalytic properties for ORR, which in turn was reflected in the performance of MSN/CB-based electrocatalysts. The study revealed that the presence of Mn species plays a key role in the ORR activity. Among tested, MSN200/CB and MSN350/CB exhibited the best electrochemical performances together with outstanding stability.

1. Introduction

Recently, the need to attain greener and safer strategies to store and use renewable energy sources has strongly contributed to the development of devices such as fuel cells or metal-air batteries (Alaswad et al., 2016; Li et al., 2017a). Therefore, the reactions involved in such devices have also attracted considerable attention, particularly, the oxygen reduction reaction (ORR) that occurs in the cathode of these devices due to its sluggish reaction kinetics, where the use of an electrocatalyst is mandatory (Dekel, 2018; Wei et al., 2020). The benchmark electrocatalysts are based on noble metal platinum (Hussain et al., 2020; Mahata et al., 2019), which is highly active for ORR. One important point of these materials is that they can be used in both acid and alkaline medium, but the latter has slightly worse stability due to Pt-leaching (Zadick et al., 2015). Such a drawback together with the high cost and scarcity of platinum foster the development of alternative materials.

Transition metal-based compounds have attracted attention to develop new electrocatalysts for ORR, since the low cost and high abundance of transition metals make them prominent candidates. Additionally, there are many straightforward methods of synthesis of metal-based materials (Osgood et al., 2016; Goswami et al., 2018). These compounds can tolerate the constant oxidation and reduction processes that occur in the electrocatalytic reactions. The transition metals can shift their cationic oxidation state that endows the transition metal-based compounds with outstanding stability (Osgood et al., 2016). Another important point of these compounds is their better stability compared to that of Pt-based electrocatalysts in alkaline medium, which is less corrosive than the acid medium, and it also offers more favorable kinetics (Firouzjaie and Mustain, 2020). Therefore, compounds such as metal oxides (Chai et al., 2017; Zhou et al., 2018), metal sulfides (Han et al., 2019a), metal nitrides (Tian et al., 2015), noble metal/transition metal hybrids (Chen et al., 2020; Zhang et al., 2020a), and bimetallic compounds (Han et al., 2019b) have been extensively studied because they exhibit excellent performance in ORR.

In this context, ferrite materials, which are mixed oxides with a cubic structure and AFe_2O_4 stoichiometry, being A a divalent cation, can be an alternative to Pt-based electrocatalysts in alkaline medium. These mixed metal oxides are considered as a platform to develop electrocatalysts for

* Corresponding author.
** Corresponding author.
*** Corresponding author.
E-mail addresses: david.salinas@ua.es (D. Salinas-Torres), mvlro@ujaen.es (M.V. López-Ramón), cmoreno@ugr.es (C. Moreno-Castilla).

https://doi.org/10.1016/j.envres.2021.112126
Received 30 July 2021; Received in revised form 17 September 2021; Accepted 17 September 2021
Available online 23 September 2021

ORR because of their tunable composition, which in turn allows the modification of their physicochemical properties. Most of the ferrites are mixed spinels (Pang and Lei, 2016), where both metal cations can be distributed in tetrahedral A sites and octahedral B sites according to the stoichiometry $[A_{1-x}^{II}B_x^{III}]^{tet}$ $[A_x^{II}B_{2-x}^{III}]^{oct}O_4$ (Kaufman et al., 1993), resulting in a structure with abundant octahedral edges and redox couple of both cations that can act as the catalytic sites for ORR (Silva et al., 2019; Samanta and Raj, 2019). Previous studies have reported that ferrite materials based on manganese (Zhou et al., 2018; Wu et al., 2018), cobalt (Samanta and Raj, 2019; Matseke et al., 2020; Bian et al., 2014) and copper (Flores-Lasluisa et al., 2020a) have electrocatalytic activity towards ORR, showing cobalt ferrites a good response in ORR due to the presence of cobalt species (Osgood et al., 2016). The manganese-based ferrites are also promising materials due to the manganese redox processes, which have shown to be excellent electrocatalytic sites, especially if the cation is in an octahedral environment (Suntivich et al., 2011; Gao and Geng, 2014; Hazarika et al., 2018). Moreover, the interaction of both Mn and Fe cations enhances the performance because the electron and energy transfer can occur between different oxidation states, facilitating redox processes on the nanoparticle surface (Deng et al., 2018).

However, the main drawbacks of the ferrites are their low surface area and low intrinsic electrical conductivity, which hamper their use as an electrocatalyst for ORR by themselves. Thereby, to mitigate both disadvantages, it is necessary to prepare metal oxide materials at a nanometer scale to modify the original properties of the bulk counterpart (Deng et al., 2016) such as the morphology, size, crystalline structure, oxidation state, the coordination of the two metal ions, and their magnetic properties, and what is more important, the increase of active surface area (Zhu et al., 2013; Gao and Geng, 2014; Zhou et al., 2018). Furthermore, as-prepared nanosized materials must be supported over materials with a good electrical conductivity to favor the electron transfer (Wu et al., 2018; Samanta and Raj, 2019; Matseke et al., 2020). At this point, carbon materials are the most prominent candidates because they fulfill the above-mentioned properties together with their chemical stability and low price. Previous studies have also claimed that carbon materials can act as co-catalysts for ORR through a two-electron transfer pathway (Poux et al., 2012; Ryabova et al., 2017; Mattick et al., 2019), generating hydrogen peroxide which can be further reduced to hydroxide by the metal oxides. Hence, the interaction of both materials produces a synergistic effect, which significantly enhances the electrocatalytic performance of metal oxides towards ORR (Li et al., 2016a; Kéranguéven et al., 2017; Flores-Lasluisa et al., 2020a).

This work has been addressed to study $MnFe_2O_4$ solid nanospheres (MSN) as auspicious electrocatalysts for ORR. MSN was prepared by a solvothermal method and calcined to different temperatures, from 200 to 500 °C to tailor their physicochemical properties (Mateus et al., 2021), which in turn lead to a different electrocatalytic performance towards ORR. MSN samples were previously characterized to know their morphology, surface area, oxidation states and coordination of Fe and Mn ions, and crystal structure and crystallite size (Mateus et al., 2021). Regarding carbon materials-mixed MSN oxides, they exhibited good electrocatalytic performance in ORR.

2. Experimental

2.1. Materials and reagents

Reagents used for the synthesis of the MSN were iron (III) nitrate nonahydrate, manganese (II) nitrate tetrahydrate, ethylene glycol, ethylenediamine, sodium acetate, and absolute ethanol, which were analytical grade reagents from Sigma-Aldrich.

A commercial carbon black (Vulcan XC-72R, Cabot Corporation, BET surface area was 255 m^2/g), potassium hydroxide (VWR Chemicals), isopropanol 99.5% (Acros. Organics), Nafion® 5% w/w water, and 1-propanol (Alfa Aesar) and 20 wt % Pt/Vulcan (Sigma-Aldrich) were also used. All solutions were prepared using ultrapure water (18 MΩ/cm from an Elga Labwater Purelab system) and the gases, N_2 (99.999%), O_2 (99.995%), and H_2 (99.999%) were provided by Air Liquide.

2.2. Synthesis procedure

MSN was prepared using a previously described method (Mateus et al., 2021: Li et al., 2016b). Briefly, $Fe(NO_3)_3.9H_2O$ (3.76 g) and $Mn(NO_3)_2.4H_2O$ (1.17 g) were dissolved in 50 mL of ethylene glycol followed by the addition of 30 mL ethylenediamine and 7.5 g sodium acetate. After magnetic stirring for 30 min, the solution was placed in a sealed Teflon-lined stainless-steel autoclave (125 mL capacity), and heated at 160 °C for 8 h before cooling down to room temperature. The brownish product was centrifuged and washed with distilled water-ethanol (1:2) three times. Finally, the resulting product was dried at 60 °C overnight. Different portions of MSN were calcined between 200 and 500 °C (5 °C min^{-1}) in an air oven for 4 h. Samples obtained will be referred to as MSN followed by the calcination temperature.

2.3. Physicochemical characterization

MSN samples were characterized by N_2 adsorption isotherms at −196 °C (Autosorb 1 from Quantachrome) to obtain their BET surface area (S_{BET}). Scanning electron microscopy (SEM) was performed with a Carl Zeiss SMT microscope and transmission electron microscopy (TEM) with a JEM-1010 microscope (JEOL).

X-ray photoelectron spectroscopy (XPS) was performed with an Escalab 200R apparatus (VG Scientific Co.) equipped with a hemispherical electron analyzer and a MgK_α X-ray source with radiation energy of 1253.6 eV. The internal standard peak to determine binding energies (BEs) was the C_{1s} peak at 284.6 eV, used to obtain the number of components, position of peaks, and peak areas. X-ray diffraction (XRD) was carried out using an X-ray Empyrean diffractometer with PIXcel-3D detector (PANanalytical, The Netherlands) as described elsewhere (López-Ramón et al., 2018). The Rietveld refinement method (Rietveld, 1969; Young et al., 1977) was applied to identify and quantify the different phases present in each sample using HighScore Plus software (Degen et al., 2014) and the Crystallography Open Database (COD) (Downs and Hall-Wallace, 2003). The average crystallite size was calculated from XRD results using the Scherrer equation.

Thermogravimetric and derivative thermogravimetry (TG-DTG) analyses were performed using a thermobalance (Mettler Toledo Star System). TG/DTG curves were recorded by heating 20 mg of MSN in an alumina crucible from 30 to 600 °C at a heating rate of 5 °C min^{-1} under an air flow of 50 mL min^{-1}.

2.4. Electrochemical characterization

The electrochemical measurements were performed in a three-electrode cell using 0.1 M KOH as electrolyte. All electrochemical data were recorded using an Autolab PGSTAT302 (Metrohm, Netherlands) potentiostat. A rotating ring-disk electrode (RRDE) from Pine Research Instruments (USA) equipped with a glassy carbon (GC) disk (5.61 mm diameter) and a Pt ring was used as a working electrode for the study of the ORR. As a counter electrode, a graphite rod was used and a reversible hydrogen electrode (RHE) immersed in the same electrolyte as the reference electrode.

For the electrochemical characterization a suspension of 1 mg of MSN materials or mixed counterparts (MSN(T)/carbon materials, 1:1 ratio and mixed in an agate mortar) in 1 mL of an aqueous Nafion-containing IPA solution (isopropanol:Nafion®; 20%:0.02% $v_/v$) was prepared by sonication. Over the glassy carbon disk, 120 μL of the dispersion was deposited and a uniform catalyst layer of 480 $\mu g/cm^2$ active material was obtained. Then, cyclic voltammetry (CV) and linear sweep voltammetry (LSV) experiments were performed to characterize all samples. In the case of CVs, the measurements were recorded from

Table 1
Surface area of MSN samples.

Sample	S_{BET} / $m^2\ g^{-1}$
MSN	138
MSN200	127
MSN350	104
MSN500	28

0 to 1 V (vs RHE) in a 0.1 M KOH solution under a nitrogen atmosphere. The ORR was studied by LSV experiments at different rotation rates (ranging from 400 to 2025 rpm) at 5 mV s^{-1} using the same potential window as CV measurements (vs RHE) in 0.1 M KOH medium; however, such measurements were performed in an O_2-saturated atmosphere. The Pt-ring potential was kept at 1.5 V during the whole LSV measurements to oxidate the hydrogen peroxide that might have been formed. Then, the percentage of hydrogen peroxide formed and the electron transfer number, n_{e^-}, were calculated by the following equations (Liu et al., 2018):

$$HO_2^-[\%] = 200x\frac{I_{ring}/N}{I_{disk} + I_{ring}/N} \quad (1)$$

$$n_{e^-} = \frac{4I_{disk}}{I_{disk} + I_{ring}/N} \quad (2)$$

where I_{disk} and I_{ring} are the currents measured at disk and ring, respectively, and N is the collection efficiency of the ring that was experimentally determined as 0.37.

The stability test was performed through chronoamperometric experiments using the RRDE at 1600 rpm in 0.1 M KOH solution under an O_2-saturated atmosphere, keeping a constant potential of 0.5 V. After 3 h of experiment, methanol was added to the background electrolyte until the concentration was 1.0 M.

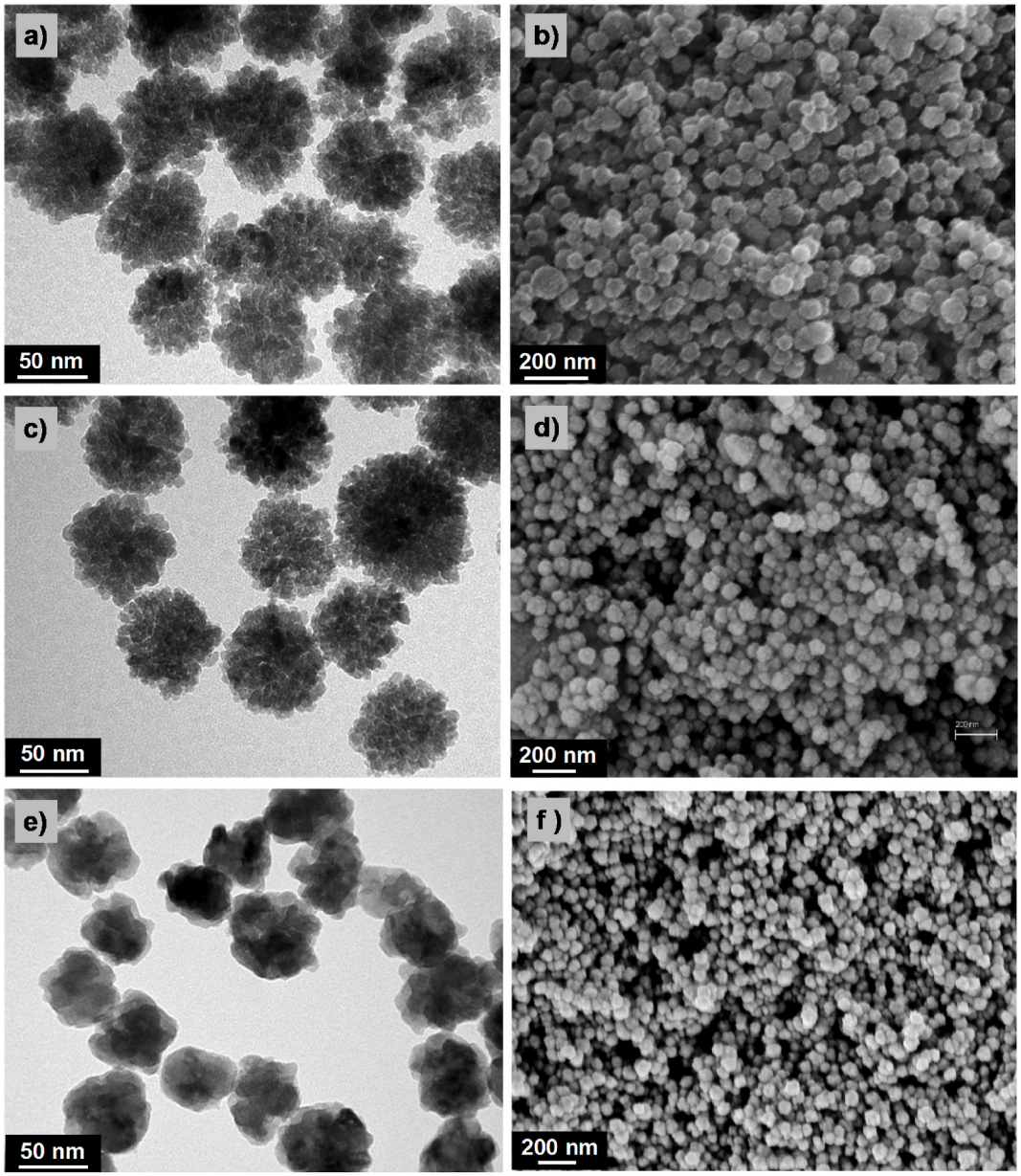

Fig. 1. TEM-SEM micrographs of (**a and b**) MSN, (**c and d**) MSN350, and (**e and f**) MSN500.

Table 2
Binding energy (eV) of the main XPS peaks of the MSN samples with percentage (in parentheses), Fe, Mn, and O atomic percentages and Mn/Fe atomic ratio.

Sample	Fe $2p_{3/2}$/eV	Mn $2p_{3/2}$/eV	Mn/Fe	Average Mn oxidation state	O $_{1s}$/eV	O_S/O_L (O_{at} %)
MSN	710.1 (32)	640.6 (65)	0.49	2.35	529.7 (71)	0.41
	711.4 (68)	641.7 (35)			531.4 (29)	(71.3)
MSN200	709.8 (31)	640.5 (63)	0.56	2.37	529.6 (71)	0.41
	711.2 (69)	641.6 (37)			531.2 (29)	(71.8)
MSN350	709.9 (30)	641.1 (66)	0.78	3.34	529.6 (73)	0.37
	711.2 (70)	642.4 (34)			531.2 (27)	(72.2)
MSN500	709.6 (28)	640.4 (18)	1.06	3.10	529.5 (71)	0.41
	711.0 (72)	641.5 (58)			531.1 (29)	(70.0)
		642.7 (25)				

3. Results and discussion

3.1. Physicochemical characterization

The physicochemical characteristics of the MSN sample and its calcined derivatives were given and widely explained in detail in a previous work (Mateus et al., 2021). So, here we will present only those characteristics that may be helpful to explain the behavior of these ferrites as electrocatalysts for ORR. S_{BET} values (Table 1) decrease with higher calcination temperature, showing a steeper reduction between 350 and 500 °C, which might result in a lower catalytic performance of MSN500 towards ORR. TEM and SEM (Fig. 1) show that samples from MSN to MSN350 are composed of nanospherical particles with an average diameter of 70–80 nm. Sample MSN500 also contains spherical particles, but its surface is smoother due to the increased calcination temperature, which explains the large reduction in S_{BET}, and the decrease of the average diameter to around 60 nm.

The surface composition of the samples plays a key role in the ORR performance. Therefore, it is necessary to determine which species are dominant on the surface. In this sense, the XPS technique was employed to distinguish the different oxidation states of the cations and their coordination. XPS profiles of the Fe 2p, Mn 2p, and O 1s core level regions are depicted in Fig. S1 a to c, respectively, of Supplementary material, and the results are compiled in Table 2. The Fe 2p spectra show two main asymmetric peaks, corresponding to the $2p_{3/2}$ and $2p_{1/2}$ signals at 710.5 and 724.2 eV, respectively, and a satellite peak at 719 eV, associated with the presence of Fe(III) on the sample surface (Wang et al., 2014; Fontecha-Cámara et al., 2016; Liu et al., 2016). The deconvolution of Fe $2p_{3/2}$ peak shows the contribution of two different species at around 709.9 and 711.2 eV, due to the presence of Fe(III) on B and A sites, respectively (Fontecha-Cámara et al., 2016; Liu et al., 2016). In addition, the percentage of Fe(III) in A sites slightly increased at high calcination temperatures, which indicates that as-synthesized manganese ferrites present a partially inverted spinel structure. This is more significant when the calcination temperature rises to 500 °C.

Mn 2p spectra (Fig. S1b) also show two asymmetric peaks at around 641.1 and 652.2 eV, corresponding to the $2p_{3/2}$ and $2p_{1/2}$ signals, and also a satellite peak at *ca.* 645 eV assigned to Mn(II). All of these results are in agreement with previous XPS findings (Liang et al., 2016; Liu et al., 2016). The $2p_{3/2}$ peak of MSN and MSN200 was deconvoluted into two peaks at around 640.6 and 641.7 eV, which are related to Mn(II) and Mn(III), respectively (Yang et al., 2011; Tang et al., 2014). When the calcination temperature increased from 200 to 350 °C the two deconvoluted peaks shifted to higher binding energies (641.1 and 642.4 eV). It confirmed the change of Mn species on the surface of MSN350 compared to MSN200. The peak at lower BE was attributed to Mn(III), while the peak located at higher BE corresponds to Mn(IV) (Yang et al., 2011; Tang et al., 2014). This change of the Mn species on the surface is due to the oxidation of Mn(II). Concerning MSN500, the $2p_{3/2}$ peak was deconvoluted into three peaks assigned to Mn(II) (640.4 eV), Mn(III) (641.5 eV), and Mn(IV) (642.7 eV). The partial reduction of Mn(IV) leads to the three contributions observed (Mateus et al., 2021). The Mn/Fe surface atomic ratio in MSN and MSN200 samples was very close to 0.5 (see Table 2), which is the theoretical value of the manganese ferrite spinel. However, this ratio increased at higher calcination temperatures, indicating that Mn was segregated to the surface of the manganese ferrite in both MSN350 and MSN500. Moreover, Table 2 shows that the average Mn oxidation state of the samples increased drastically up to 350 °C, and then it decreased slightly. Among the different samples, it could be expected that MSN350 exhibits a better electrocatalytic performance because its average Mn oxidation state is close to the optimum value (~3.4), which produces a suitable Mn-oxygen interaction (Stoerzinger et al., 2015; Wei et al., 2017).

Fig. S1c shows the deconvolution of the O 1s peak that resulted into two other peaks at around 529.6 and 531.2 eV (Table 2), due to the surface lattice oxygen (O_L) and surface hydroxide species (OH^-) (O_S), respectively (Kester et al., 1997; Yang et al., 2011; Liang et al., 2016). The latter oxygen groups play an important role in the ORR mechanism, for this reason, it will be discussed latter in more detail. The total surface oxygen concentration (O_{at} % in Table 2) increased up to 350 °C, what can be due to the oxidation of Mn(II) to Mn(III) and Mn(IV), and then decreased above 350 °C due to the reduction process of Mn species (Mateus et al., 2021).

Fig. S2 depicts the TG/DTG curves which reveal three stages. The first stage, up to around 240 °C, shows a weight loss of 3.9% and an endothermic band at around 150 °C associated to dehydration and dehydroxylation processes (Mateus et al., 2021). The second stage, between 240 and 364 °C shows a weight increase of around 0.4% and an exothermic band which are due to the partial oxidation of Mn(II) to Mn (III) and Mn(IV) (Mateus et al., 2021). Finally, the third stage, between 364 and 600 °C shows a weight loss of 2.5% and two endothermic bands at around 420 and 500 °C attributed to the spinel dehydroxylation, which reduces Mn(IV) to Mn(III) and Mn(II). These findings are supported by the XPS results.

In summary, results obtained show that: firstly, B sites are preferentially occupied by Mn(III) and Mn(IV) ions as the calcination temperature increases. This is attributable either to the oxidation of previous Mn(II) ions in B sites or to the substitution of Fe(III) in these sites by Mn(III) or Mn(IV), which are more favored to occupy them than Fe(III) due to their crystal field stabilization energy (Atkins et al., 2010). Metal ions present in the B sites of ferrites are highly important in all phenomenon that occurs on their surface because they are directly exposed to it (Deng et al., 2016). Secondly, MSN350 has the highest amount of Mn(III) in such sites, and also the highest amount of total and lattice oxygen, which would favor the oxygen mobility for Mn redox cycles (Mateus et al., 2021).

The crystal structure of the oxide materials may influence the ORR performance since the interaction between the active sites and the reactants depends on the structure. The XRD patterns of the samples are depicted in Fig. S3, and their results are compiled in Table 3. MSN and

Table 3
Crystalline phases, lattice parameters and crystallite sizes of MSN samples obtained from XRD patterns.

Sample	Crystalline phase	Lattice parameter (nm)	Crystallite size (nm)
MSN	Jacobsite	0.83931	10.2
MSN200	Jacobsite	0.83651	6.0
MSN350	Maghemite	0.83234	8.0
MSN500	Maghemite	0.83530	8.9

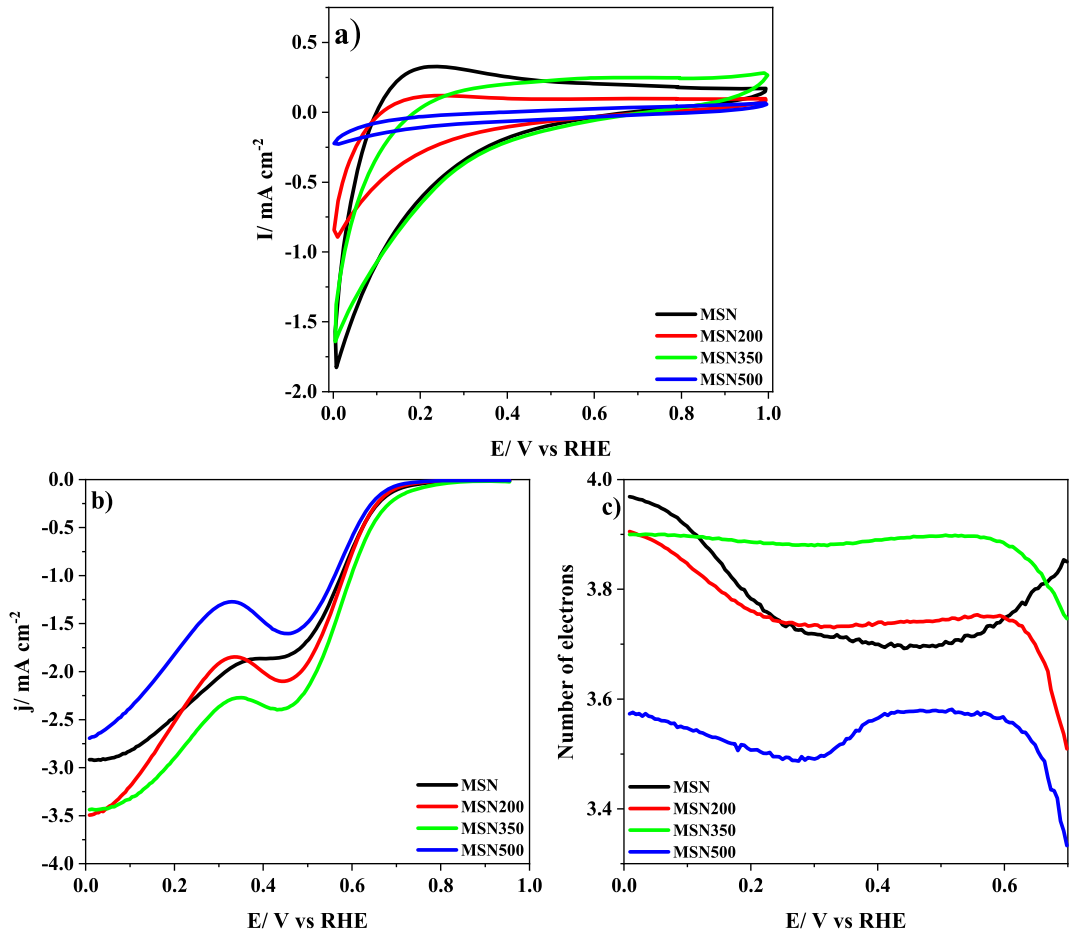

Fig. 2. Cyclic voltammograms of MSN samples deposited on glassy carbon substrates in 0.1 M KOH medium saturated with N_2. Scan rate: 50 mV s^{-1}. **b)** Linear sweep voltammograms recorded at 1600 rpm for MSN samples in O_2-saturated 0.1 M KOH solution. Scan rate: 5 mV s^{-1}; **c)** Electron transfer numbers calculated from the current measured at the ring using Eq. (2).

MSN200 display the typical patterns of the cubic spinel jacobsite, whereas MSN350 and MSN500 show a maghemite structure (Yang et al., 2011; Liang et al., 2016), which is a non-stoichiometric spinel $MnFe_2O_{4+\delta}$ (Kester et al., 1997; Mateus et al., 2021). The lattice parameter (Table 3) variations are due to the decrease in Mn radius at higher oxidation states, e.g., Mn(II) 0.097 nm, Mn(III) 0.072 nm, and Mn (IV) 0.067 nm in the same B site coordination (Liang et al., 2016). Thus, XPS results showed that the percentage of Mn(III) and Mn(IV) increased from MSN to MSN350 and that the percentage of Mn(IV) decreased in MSN500, with the reappearance of Mn(II) (Mateus et al., 2021).

The mean crystallite size decreased from MSN to MSN200 and then increased up to MSN500. However, the difference is not that important, so other parameters would be more important in the ORR catalytic performance of the samples such as the S_{BET} or the surface chemistry.

3.2. Electrochemical characterization

The different calcination temperature employed on the MSN sample modifies their original physicochemical properties, so it could be expected that such changes influence the electrochemical properties, which in turn would affect the electrocatalytic behavior towards ORR. Firstly, the samples were characterized by cyclic voltammetry in saturated N_2 or O_2 atmospheres. Then, the electroactivity of all samples was tested using a RRDE. Moreover, to enhance the electrocatalytic performance of the oxide materials, they were mixed with carbon black (CB) to prepare MSN(T)/CB materials, which were also studied using the same procedure.

3.2.1. MSN-based materials

The MSN samples exhibit different electrochemical behavior depending on the calcination temperature. Fig. 2a displays the cyclic voltammograms of the samples in 0.1 M KOH under a N_2-saturated atmosphere. It can be observed that samples have similar electrochemical response with the absence of redox processes and the voltametric current decreases with the calcination temperature. Then, the samples with the higher apparent surface area have similar profile, whereas the MSN500 sample exhibits the lowest voltammetric charge, which might be related to its lower S_{BET} that limits the number of available surface-active sites. Mn redox processes should be detected for this potential window; however, no redox peaks are recorded. This fact might be related to the low electrical conductivity of the samples, which would hinder a good electron transfer between the oxide particles and the current collector.

To assess the electrocatalytic performance of the MSN-based samples towards ORR, polarization curves were recorded using an RRDE in 0.1 KOH under an oxygen atmosphere. Fig. 2b shows the linear sweep voltammograms for the MSN samples. Two well-differentiated reduction processes can be distinguished. The first reduction process, that involves only dioxygen, starts at around 0.7 V and finishes at around 0.5 V, whereas the second reduction process occurs between 0.3 V and 0.1 V and is related to the reduction of both dioxygen and hydrogen peroxide (Flores-Lasluisa et al., 2020b). Fig. 2c displays the number of electrons involved at each potential. As it can be noted, the number of electrons at 0.6 V is quite close to the desired 4-electron pathway (3.6–3.9), but it differs from the samples depending on the calcination temperature, showing the lowest number of electrons the sample calcinated at 500 °C,

Table 4
Onset potential, number of electrons, limiting current density, and Tafel slope obtained for the ORR reaction at MSN-based samples.

Sample	E_{onset} /V (at −0.10 mA cm^{-2})	n_{e^-} (at 0.4 V vs RHE)	j_{lim} /mA cm^{-2} (at 0.4 V)	Tafel slope/ mV dec^{-1}
MSN	0.70	3.70	−1.86	112
MSN200	0.70	3.74	−2.00	99
MSN350	0.75	3.89	−2.35	162
MSN500	0.68	3.56	−1.46	94

and the highest the sample treated at 350 °C.

Different electrochemical reactions can proceed depending on the overpotential region. The 4-electron and the 2-electron dioxygen reduction (peroxide formation) can occur at lower overpotential, while the hydrogen peroxide generated by the 2-electron pathway can suffer a further chemical disproportionation reaction or can be reduced by a 2-electron pathway to hydroxide ions at higher overpotentials (Mattick et al., 2018, 2019).

Table 4 summarizes the electrochemical parameters obtained for the MSN-based samples. The different performance of the samples in the ORR might be ascribed to the different S_{BET} and transition metal surface concentrations of the samples, which have shown a strong catalytic effect on the electrochemical reaction (Stoerzinger et al., 2015). The ORR in metal oxides materials can proceed by a 4-electron pathway that consists of a multi-step process. Before discussing the mechanism, it is important to mention that surface B cations adopt a square pyramidal symmetry and, rather than being surrounded by 6 oxygen anions, they are only surrounded by five oxygens, leaving an empty position that would be used to interact with the reactants and products. Therefore, the surface hydroxide groups, which were detected by XPS, are located in the empty position and may participate in the following ORR mechanism: (i) displacement of adsorbed hydroxide by oxygen molecule, (ii) surface hydroperoxide formation, (iii) surface oxide formation, and (iv) adsorbed hydroxide regeneration (Suntivich et al., 2011; Li et al., 2015). The mechanism involves the interaction of the e_g orbital of the transition metal in an octahedral environment with the oxygen orbital, and it is required an occupancy of one electron in the e_g orbital for the easier displacement of the adsorbed hydroxide by the oxygen molecule (rate-limiting step). Among both transition metals, Mn(III) in octahedral sites is the most active cation site for the ORR mechanism because it contains one electron in the e_g orbital that results in an increased ORR reaction rate (Hong et al., 2015).

Moreover, previous studies have reported the beneficial effect of Mn (IV) for the ORR due to its higher oxidative ability compared to Mn(III) (Hu et al., 2015; Zhao et al., 2018). Thus, the hydrogen peroxide reduction can be boosted by the presence of Mn(IV) through the chemical disproportionation reaction, enhancing the overall ORR performance. Moreover, the presence of Mn(IV) can increase the covalency of the metal-oxygen bond and facilitate the electron transfer in the O_2/OH^- exchange (surface hydroxide displacement) (Long et al., 2019; Lv et al., 2019). However, the Mn(IV) concentration must be low to avoid interfering with the number of Mn(III) species active sites. Moreover, the suitable crystal structure would not undergo a significant distortion. It might lead to the enhancement of the overall reaction kinetics. Despite MSN350 and MSN500 contain Mn(IV) species, it only seems to affect positively in the MSN350, whereas the MSN500 exhibited the worst ORR performance, which might be associated with its low surface area that limits the number of available active sites.

According to the electrochemical parameters, the samples do not exhibit large differences in their ORR performance but, among them, the MSN350 sample displayed the best ORR performance, which is related to its Mn surface concentration that provides a greater number of available active sites. However, this sample has the worst kinetics as it can be observed from its high Tafel slope value. This can be related to its lower surface hydroxide concentration, which might hinder the electron transfer in the first step of the mechanism. The high value of the Tafel slopes indicates that the first electron transfer seems to be the rate-determining step, i.e., the replacement of hydroxide species by oxygen molecules (Shinagawa et al., 2015).

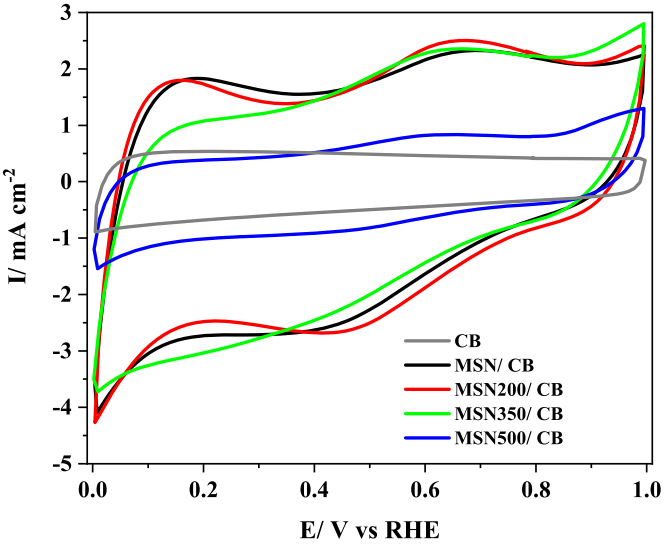

Fig. 3. Cyclic voltammograms of MSN/CB materials deposited on glassy carbon substrates in 0.1 M KOH medium saturated with N_2. Scan rate: 50 mV s^{-1}.

3.2.2. *MSN-based materials mixed with carbon black*

Previous studies have reported the importance of mixing carbon materials with metal oxide materials due to the enhancement in the electrical conductivity in the resulting materials compared to that of the metal oxide counterparts (Kéranguéven et al., 2015, 2017; Flores-Lasluisa et al., 2020b). Additionally, the carbon material can act as a co-catalyst, and a synergistic effect between the metal oxide material and the carbon material might occur, which could facilitate the electron transfer, improving the overall ORR. The mixture between both materials was performed using a metal oxide/carbon material ratio of 1:1 (Flores-Lasluisa et al., 2020b).

The MSN-based materials physically mixed with carbon black and the pristine carbon black were electrochemically characterized by cyclic voltammetry and the results are depicted in Fig. 3. In the potential window studied, the carbon black does not exhibit any redox process and it only exhibits double-layer charging processes. It can be observed that the materials MSN/CB and MSN200/CB have a similar double-layer capacitance. The MSN350/CB material has a slight decrease of the double-layer capacitance; however, the MSN500/CB material has a sharp decrease in the capacitance, which might be related to its lower S_{BET} that limits the number of accessible metal oxide surface sites.

The presence of the carbon black material increases the double-layer capacitance and favours the appearance of redox peaks from the metal oxides because it improves the electrical conductivity and the electron transfer between the metal oxide particles and the current collector (glassy carbon electrode) (Kéranguéven et al., 2017). Fig. 3 shows the CVs recorded in an N_2-atmosphere and some peaks can be observed related to the transition metal redox processes. In the case of Mn, peaks related to the Mn(II)/Mn(III) redox processes in the anodic and cathodic scans appear at around 0.65 and 0.4, respectively (Celorrio et al., 2016; Flores-Lasluisa et al., 2020b). Moreover, the increase in the current density above 0.8 V might indicate the formation of Mn(IV) in all materials. In addition, it is observed the Fe(III) reduction starts at around 0.1 V, showing an increase in the cathodic current density in the case of MSN-based materials mixed with carbon black (Guan et al., 2013). This cathodic current is less intense as the Fe surface concentration decreases (i.e., as it increases Mn/Fe ratio in Table 2).

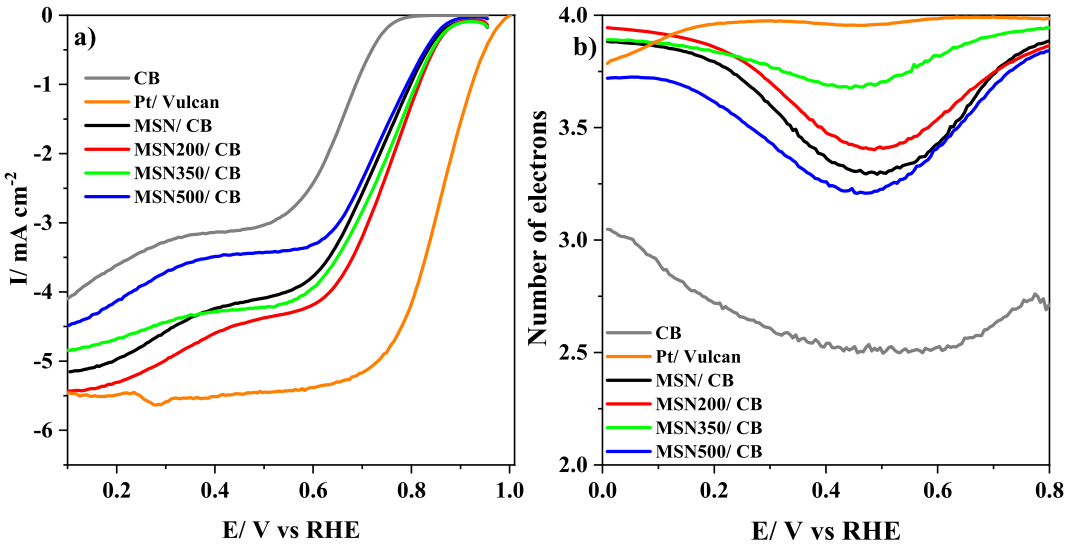

Fig. 4. **a)** Linear sweep voltammograms recorded at 1600 rpm for MSN/CB materials in O_2-saturated 0.1 M KOH solution. Scan rate: 5 mV s^{-1}; **b)** Electron transfer numbers calculated from the current measured at the ring using Eq. (2).

Table 5
Onset potential, number of electrons, limiting current density and Tafel slope obtained for the ORR reaction at MSN/CB.

Sample	E_{onset} /V (at −0.10 mA cm^{-2})	n_{e^-} (at 0.7 V vs RHE)	j_{lim} /mA cm^{-2} (at 0.4 V)	Tafel slope/ mV dec^{-1}
MSN/CB	0.90	3.74	−4.24	86
MSN200/ CB	0.90	3.75	−4.60	73
MSN350/ CB	0.91	3.91	−4.29	82
MSN500/ CB	0.88	3.69	−3.49	68
Pt/Vulcan	0.98	3.99	−5.51	60
Carbon black	0.77	2.53	−3.14	62

Table 6
Onset potential, number of electrons, limiting current density, and Tafel slope obtained for the ORR reaction at MSN/CB.

Sample	E_{onset} /V	Electron number	j_{lim} /mA cm^{-2}	Tafel slope/ mV dec^{-1}
MSN200/CB (This work)	0.90	3.75	−4.60	73
MSN350/CB (This work)	0.91	3.91	−4.29	82
CFNS400/CB (Flores-Lasluisa et al., 2020a)	0.82	3.53	−4.95	80
$LaMn_{0.7}Co_{0.3}O_3$/CB (Flores-Lasluisa et al., 2020b)	0.84	3.78	−4.82	81
Co_3O_4/NCNTs/3D graphene (Liu et al., 2020)	0.89	3.97	–	66
$NiCo_2O_4$/CB (Béjar et al., 2019)	0.91	3.83	−3.42	89
rGO/$CoFe_2O_4$ (Samanta and Raj, 2019)	0.85	3.9	–	63
$CoFe_2O_4$/rGO (Bian et al., 2014)	0.89	3.85	–	67
Fe_3O_4/N-doped carbon (Li et al., 2017b)	0.96	3.5	–	77
Defected Mn_3O_4 (Zhang et al., 2020b)	0.87	3.96	−5.00	101
Co_3O_4/N-rmGO (Liang et al., 2011)	~0.90	4	−5.00	42

The electroactivity of the MSN/CB materials was tested using the same method described before for MSN samples. The results obtained are displayed in Fig. 4 together with carbon black and 20 wt %Pt/Vulcan for comparison purposes. As expected, the carbon black sample exhibits the worst electrocatalytic response in ORR, whereas the 20%Pt/Vulcan has the best electrocatalytic performance due to the presence of Pt active sites. Fig. 4a shows the polarization curves for the metal oxide-based materials and it can be noted that all the MSN mixed with carbon black have a similar onset potential, but with a different limiting current density which is related to the different number of electrocatalytic active sites. On the other hand, the number of transferred electrons by which occurs the ORR (Fig. 4b) is again close to the 4-electron pathway (3.4–3.8 at 0.6 V), showing a slightly different pathway between the materials.

The electrochemical parameters obtained from the LSV plots are summarized in Table 5. As was expected, the MSN500/CB material has a slightly worse electrocatalytic performance in ORR compared to the other materials, which might be related to the lower apparent surface area of the metal oxide material that limits the number of catalytic active sites towards ORR. It can be confirmed that the calcination treatment up to 350 °C has a positive effect on electrochemical parameters such as the number of electrons or limiting current density. This improvement is ascribed to an increase of the catalytic Mn species together with the reduction of the nanoparticles size, especially in MSN200/CB that provides a higher number of active sites to participate in the ORR. Among the different MSN mixed with carbon black materials, the MSN350/CB has the best ORR performance, which might be related to the significant concentration of Mn(III) and an optimum amount of Mn(IV) which gives the average Mn oxidation state value close to the optimum value (~3.4, Table 2), which produces a suitable Mn-oxygen interaction for this reaction (Stoerzinger et al., 2015; Wei et al., 2017).

In the case of the value of the Tafel slopes, they are smaller compared to the MSN samples due to an enhancement of the kinetics by the presence of carbon black that improves the electrical conductivity and facilitates the electron transfer. With the exception of the MSN500/CB sample, the MSN mixed with carbon black present again, as rate-limiting step, the replacement of hydroxide species by oxygen molecules because their Tafel values are close to 90 mV dec^{-1}, whereas for the MSN500/CB material its value of 68 mV cm^{-1} (close to 60 mV cm^{-1}) indicates that the rate-limiting step is the peroxide reduction to yield OH^- (Hong et al., 2015). The comparison of the electrochemical behavior towards the ORR of our high-performing electrocatalysts with other metal oxide-based electrocatalysts reported in the literature can be found in

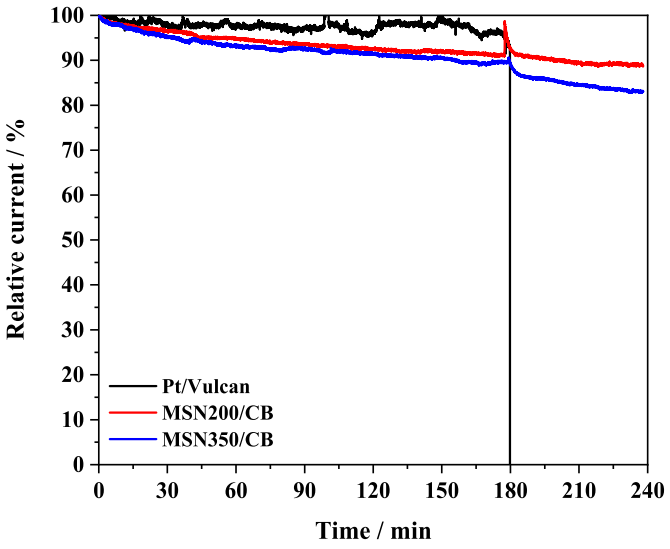

Fig. 5. Comparative stability test for MSN200/CB and 20% Pt/Vulcan carried out at 0.5 V and 1600 rpm in O_2-saturated 0.1 M KOH and 25 °C. Methanol was added 180 min after launching the experiment.

Table 6.

The good performance of these metal oxides towards ORR makes them promising electrocatalysts in ORR. Therefore, it is compulsory to analyze their stability. In this case, the MSN200/CB and MSN350/CB samples were selected to evaluate their stability by chronoamperometric measurements using the RRDE at 1600 rpm in O_2-saturated electrolyte at a constant potential of 0.5 V (Liu et al., 2017). The stability of these materials was compared to a commercial 20 wt % Pt/Vulcan electrocatalyst. The Pt-based catalyst shows a current retention close to 95%; however, in the presence of methanol, the current drops to zero due to the poisoning of the Pt active sites by the CO produced in the methanol oxidation reaction (MOR). On the contrary, the MSN200/CB and MSN350/CB materials show a slow decrease of the initial activity after 3 h giving a current retention of around 90% (see Fig. 5). The samples display much better methanol tolerance decreasing slightly the current retention reaching up to 89 and 83% (see Fig. 5) for the MSN200/CB and MSN350/CB materials, respectively. Within both materials, the MSN200/CB shows a better stability with and without the presence of methanol. This might be related to the higher Mn surface concentration and, especially, to the concentration of Mn(III). In the case of MSN350/CB material, most of Mn species remain as Mn(III) and Mn (IV) and no Mn(II) is detected. It was reported in previous studies for Mn-based materials (Mefford et al., 2014) that Mn(III) could be oxidized to Mn(IV) at the potential used in the stability test. Therefore, the loss of catalytic activity with the time at a constant potential could be related to the oxidation of the Mn(III) catalytic sites, which are present in a high concentration in MSN350/CB sample.

4. Conclusions

A set of MSN materials have been prepared by a solvothermal method and then they were calcined at different temperatures ranging from 200 to 500 °C. MSN and MSN200 showed a jacobsite structure, Mn in oxidation states (II) and (III) and a Mn/Fe surface atomic ratio close to two. MSN350 and MSN500 had a maghemite structure with Mn in oxidation states (III) and (IV), and (II), (III) and (IV), respectively. Both samples showed a Mn/Fe surface atomic ratio higher than 2, indicative of a Mn surface segregation with increasing temperature above 200 °C.

The MSN materials exhibited a low performance in ORR because of their low electrical conductivity. The electrocatalytic response was influenced by the beneficial effect of the presence of Mn(IV) as it was observed for MSN350 with exhibits an average Mn oxidation state value close to the optimum value for the ORR.

Regarding MSN-based materials mixed with carbon black, they displayed a promising electrocatalytic activity towards ORR, which was ascribed to the improved electrical conductivity and electron transfer of the MSN/CB materials. Additionally, Vulcan might be acting as a co-catalyst, thus improving the overall ORR. The high-performing electrocatalysts were MSN200/CB and MSN350/CB. The last one presented a significant concentration of Mn (III) species and suitable Mn (IV) content, which depicted the most active materials towards ORR. Among assessed MSN/CB materials, MSN200/CB exhibited the best electrocatalytic activity, good stability, and a better methanol tolerance.

Declaration of competing interest

The authors declare that they have no known competing financial interests or personal relationships that could have appeared to influence the work reported in this paper.

Acknowledgements

Authors from the Universidad de Alicante acknowledge to the Ministerio de Ciencia e Innovación (PID2019–105923RB-I00) for financial support. J.X.F.-L. gratefully acknowledges (MINECO for the financial support through an FPI contract (BES-2017-081598). D.S.-T. thanks MICINN for the "Juan de la Cierva" contract (IJCI-2016-27636). M.V.L.-R. and C.M.-C. acknowledge to Junta de Andalucía, projects RNM366 and RNM172, respectively.

Appendix A. Supplementary data

Supplementary data to this article can be found online at https://doi.org/10.1016/j.envres.2021.112126.

Credit author statement

J.X. F.-L.: Conceptualization, Methodology, Investigation, Writing – original draft, Funding acquisition. D.S.-T.: Conceptualization, Methodology, Investigation, Writing – original draft, Funding acquisition. M. V.L.-R.: Conceptualization, Methodology, Investigation, Writing – review & editing. C. M.-C.: Conceptualization, Methodology, Investigation, Writing – review & editing. M.A.Á.: Conceptualization, Methodology, Investigation, Writing – review & editing. E M.: Conceptualization, Methodology, Project administration, Supervision, Writing – review & editing, Funding acquisition. D.C.-A.: Conceptualization, Methodology, Supervision, Writing – review & editing.

References

Alaswad, A., Baroutaji, A., Achour, H., Carton, J., Al Makky, A., Olabi, A.G., 2016. Developments in fuel cell technologies in the transport sector. Int. J. Hydrogen Energy 41, 16499–16508. https://doi.org/10.1016/j.ijhydene.2016.03.164.

Atkins, P., Overton, T., Rourke, J., Weller, M., Armstrong, F., 2010. Inorganic Chemistry, fifth ed. Oxford University Press.

Béjar, J., Álvarez-Contreras, L., Ledesma-García, J., Arjona, N., Arriaga, L.G., 2019. Electrocatalytic evaluation of Co_3O_4 and $NiCo_2O_4$ rosettes-like hierarchical spinel as bifunctional materials for oxygen evolution (OER) and reduction (ORR) reactions in alkaline media. J. Electroanal. Chem. 847, 113190. https://doi.org/10.1016/j.jelechem.2019.113190.

Bian, W., Yang, Z., Strasser, P., Yang, R., 2014. A $CoFe_2O_4$/graphene nanohybrid as an efficient bi-functional electrocatalyst for oxygen reduction and oxygen evolution. J. Power Sources 250, 196–203. https://doi.org/10.1016/j.jpowsour.2013.11.024.

Celorrio, V., Dann, E., Calvillo, L., Morgan, D.J., Hall, S.R., Fermin, D.J., 2016. Oxygen reduction at carbon-supported lanthanides: the role of the B-site. ChemElectroChem 3, 283–291. https://doi.org/10.1002/celc.201500440.

Chai, H., Xu, J., Han, J., Su, Y., Sun, Z., Jia, D., Zhou, W., 2017. Facile synthesis of Mn_3O_4-rGO hybrid materials for the high-performance electrocatalytic reduction of oxygen. J. Colloid Interface Sci. 488, 251–257. https://doi.org/10.1016/j.jcis.2016.10.049.

Chen, Y., Shi, Z., Li, S., Feng, J., Pang, B., Yu, L., Zhang, W., Dong, L., 2020. N, S-codoped graphene supports for Ag-$MnFe_2O_4$ nanoparticles with improved performance for

oxygen reduction and oxygen evolution reactions. J. Electroanal. Chem. https://doi.org/10.1016/j.jelechem.2020.113930, 860113930.
Degen, T., Sadki, M., Bron, E., König, U., Nénert, G., 2014. The HighScore suite. Powder Diffr. 29, S13–S18. https://doi.org/10.1017/S0885715614000840.
Dekel, D.R., 2018. Review of cell performance in anion exchange membrane fuel cells. J. Power Sources 375, 158–169. https://doi.org/10.1016/j.jpowsour.2017.07.117.
Deng, J., Feng, S., Ma, X., Tan, C., Wang, H., Zhou, S., Zhang, T., Li, J., 2016. Heterogeneous degradation of Orange II with peroxymonosulfate activated by ordered mesoporous $MnFe_2O_4$. Separ. Purif. Technol. 167, 181–189. https://doi.org/10.1016/j.seppur.2016.04.035.
Deng, J., Xu, M., Qiu, C., Chen, Y., Ma, X., Gao, N., Li, X., 2018. Magnetic $MnFe_2O_4$ activated peroxymonosulfate processes for degradation of bisphenol A: performance, mechanism and application feasibility. Appl. Surf. Sci. 459, 138–147. https://doi.org/10.1016/j.apsusc.2018.07.198.
Downs, M., Hall-Wallace, R.T., 2003. The American Mineralogist crystal structure database. Am. Mineral. 88, 247–250. http://link.springer.com/10.1007/978-3-642-00207-6_5.
Firouzjaie, H.A., Mustain, W.E., 2020. Catalytic advantages, challenges, and priorities in alkaline membrane fuel cells. ACS Catal. 10, 225–234. https://doi.org/10.1021/acscatal.9b03892.
Flores-Lasluisa, J.X., Salinas-Torres, D., López-Ramón, M.V., Álvarez, M.A., Moreno-Castilla, C., Cazorla-Amorós, D., Morallón, E., 2020a. Copper ferrite nanospheres composites mixed with carbon black to boost the oxygen reduction reaction. Colloids Surf. A Phys. Eng. Asp. 613, 126060. https://doi.org/10.1016/j.colsurfa.2020.126060.
Flores-Lasluisa, J.X., Huerta, F., Cazorla-Amorós, D., Morallon, E., 2020b. Carbon material and cobalt-substitution effects in the electrochemical behavior of $LaMnO_3$ for ORR and OER. Nanomaterials 10, 2394. https://doi.org/10.3390/nano10122394.
Fontecha-Cámara, M.A., Moreno-Castilla, C., López-Ramón, M.V., Álvarez, M.A., 2016. Mixed iron oxides as Fenton catalysts for gallic acid removal from aqueous solutions. Appl. Catal. B Environ. 196, 207–215. https://doi.org/10.1016/j.apcatb.2016.05.032.
Gao, S., Geng, K., 2014. Facile construction of Mn_3O_4 nanorods coated by a layer of nitrogen-doped carbon with high activity for oxygen reduction reaction. Nanomater. Energy 6, 44–50. https://doi.org/10.1016/j.nanoen.2014.02.013.
Goswami, C., Hazarika, K.K., Bharali, P., 2018. Transition metal oxide nanocatalysts for oxygen reduction reaction. Mater. Sci. Energy Technol. 1, 117–128. https://doi.org/10.1016/j.mset.2018.06.005.
Guan, D., Gao, Z., Yang, W., Wang, J., Yuan, Y., Wang, B., Zhang, M., Liu, L., 2013. Hydrothermal synthesis of carbon nanotube/cubic Fe_3O_4 nanocomposite for enhanced performance supercapacitor electrode material. Mater. Sci. Eng. B Solid-State Mater. Adv. Technol. 178, 736–743. https://doi.org/10.1016/j.mseb.2013.03.010.
Han, X., Zhang, W., Ma, X., Zhong, C., Zhao, N., Hu, W., Deng, Y., 2019a. Identifying the activation of bimetallic sites in $NiCo_2S_4$@g-C_3N_4-CNT hybrid electrocatalysts for synergistic oxygen reduction and evolution. Adv. Mater. 31, 1808281. https://doi.org/10.1002/adma.201808281.
Han, X., Ling, X., Yu, D., Xie, D., Li, L., Peng, S., Zhong, C., Zhao, N., Deng, Y., Hu, W., 2019b. Atomically dispersed binary Co-Ni sites in nitrogen-doped hollow carbon nanocubes for reversible oxygen reduction and evolution. Adv. Mater. 31, 1905622. https://doi.org/10.1002/adma.201905622.
Hazarika, K.K., Goswami, C., Saikia, H., Borah, B.J., Bharali, P., 2018. Cubic Mn_2O_3 nanoparticles on carbon as bifunctional electrocatalyst for oxygen reduction and oxygen evolution reactions. Mol. Catal. 451, 153–160. https://doi.org/10.1016/j.mcat.2017.12.012.
Hong, W.T., Risch, M., Stoerzinger, K.A., Grimaud, A., Suntivich, J., Shao-Horn, Y., 2015. Toward the rational design of non-precious transition metal oxides for oxygen electrocatalysis. Energy Environ. Sci. 8, 1404–1427. https://doi.org/10.1039/C4EE03869J.
Hu, J., Wang, L., Shi, L., Huang, H., 2015. Oxygen reduction reaction activity of $LaMn_{1-x}Co_xO_3$-graphene nanocomposite for zinc-air battery. Electrochim. Acta 161, 115–123. https://doi.org/10.1016/j.electacta.2015.02.048.
Hussain, S., Erikson, H., Kongi, N., Sarapuu, A., Solla-Gullón, J., Maia, G., Kannan, A.M., Alonso-Vante, N., Tammeveski, K., 2020. Oxygen reduction reaction on nanostructured Pt-based electrocatalysts: a review. Int. J. Hydrogen Energy 45, 31775–31797. https://doi.org/10.1016/j.ijhydene.2020.08.215.
Kaufman, G.B., 1993. Inorganic chemistry: principles of structure and reactivity. 4th ed. (Huheey, James E.; Keiter, Ellen A.; Keiter, Richard L.). J. Chem. Educ. 70, A279. https://doi.org/10.1021/ed070pA279.1.
Kéranguéven, G., Royer, S., Savinova, E., 2015. Synthesis of efficient Vulcan-$LaMnO_3$ perovskite nanocomposite for the oxygen reduction reaction. Electrochem. Commun. 50, 28–31. https://doi.org/10.1016/j.elecom.2014.10.019.
Kéranguéven, G., Ulhaq-Bouillet, C., Papaefthimiou, V., Royer, S., Savinova, E., 2017. Perovskite-carbon composites synthesized through in situ autocombustion for the oxygen reduction reaction: the carbon effect. Electrochim. Acta 245, 156–164. https://doi.org/10.1016/j.electacta.2017.05.113.
Kester, A., Perriat, E., Gillot, P., Tailhades, B., Rousset, B., 1997. Correlation between oxidation states of transition metal ions and variation of the coercivity in mixed-valence defect spinel ferrites. Solid State Ionics 101–103, 457–463. https://doi.org/10.1016/S0167-2738(97)84068-4.
Li, C., Han, X., Cheng, F., Hu, Y., Chen, C., Chen, J., 2015. Phase and composition controllable synthesis of cobalt manganese spinel nanoparticles towards efficient oxygen electrocatalysis. Nat. Commun. 6, 1–8. https://doi.org/10.1038/ncomms8345.
Li, T., Liu, J., Jin, X., Wang, F., Song, Y., 2016a. Composition-dependent electro-catalytic activities of covalent carbon-$LaMnO_3$ hybrids as synergistic catalysts for oxygen reduction reaction. Electrochim. Acta 198, 115–126. https://doi.org/10.1016/j.electacta.2016.02.027.
Li, M., Gao, Q., Wang, T., Gong, Y.-S., Han, B., Xia, K.-S., Zhou, C.-G., 2016b. Solvothermal synthesis of $Mn_xFe_{3-x}O_4$ nanoparticles with interesting physicochemical characteristics and good catalytic degradation activity. Mater. Des. 97, 341–348. https://doi.org/10.1016/j.matdes.2016.02.103.
Li, L., wen Chang, Z., Zhang, X.B., 2017. Recent progress on the development of metal-air batteries. Adv. Sustain. Syst. 1, 1–51. https://doi.org/10.1002/adsu.201700036.
Li, G.-L., Liu, C.-D., Chen, S.-M., Hao, C., Cheng, G.-C., Xie, Y.-Y., 2017. Promotion of oxygen reduction performance by Fe_3O_4 nanoparticles support nitrogen-doped three dimensional meso/macroporous carbon based electrocatalyst. Int. J. Hydrogen Energy 42, 4133–4145. https://doi.org/10.1016/j.ijhydene.2016.10.081.
Liang, Y., Li, Y., Wang, H., Zhou, J., Wang, J., Regier, T., Dai, H., 2011. Co_3O_4 nanocrystals on graphene as a synergistic catalyst for oxygen reduction reaction. Nat. Mater. 10, 780–786. https://doi.org/10.1038/nmat3087.
Liang, X., Liu, P., He, H., Wei, G., Chen, T., Tan, W., Tan, F., Zhu, J., Zhu, R., 2016. The variation of cationic microstructure in Mn-doped spinel ferrite during calcination and its effect on formaldehyde catalytic oxidation. J. Hazard Mater. 306, 305–312. https://doi.org/10.1016/j.jhazmat.2015.12.035.
Liu, P., He, H., Wei, G., Liang, X., Qi, F., Tan, F., Tan, W., Zhu, J., Zhu, R., 2016. Effect of Mn substitution on the promoted formaldehyde oxidation over spinel ferrite: catalyst characterization, performance and reaction mechanism. Appl. Catal. B Environ. 182, 476–484. https://doi.org/10.1016/j.apcatb.2015.09.055.
Liu, K., Li, J., Wang, Q., Wang, X., Qian, D., Jiang, J., Li, J., Chen, Z., 2017. Designed synthesis of $LaCoO_3$/N-doped reduced graphene oxide nanohybrid as an efficient bifunctional electrocatalyst for ORR and OER in alkaline medium. J. Alloys Compd. 725, 260–269. https://doi.org/10.1016/j.jallcom.2017.07.178.
Liu, X., Gong, H., Wang, T., Guo, H., Song, L., Xia, W., Gao, B., Jiang, Z., Feng, L., He, J., 2018. Cobalt-doped perovskite-type oxide $LaMnO_3$ as bifunctional oxygen catalysts for hybrid lithium-oxygen batteries. Chem. - An Asian J. 13, 528–535. https://doi.org/10.1002/asia.201701561.
Liu, Y., Yang, L., Xie, B., Zhao, N., Yang, L., Zhan, F., Pan, Q., Han, J., Wang, X., Liu, J., Li, J., Yang, Y., 2020. Ultrathin Co_3O_4 nanosheet clusters anchored on nitrogen doped carbon nanotubes/3D graphene as binder-free cathodes for Al-air battery. Chem. Eng. J. 381, 122681. https://doi.org/10.1016/j.cej.2019.122681.
Long, X., Yu, P., Zhang, N., Li, C., Feng, X., Ren, G., Zheng, S., Fu, J., Cheng, F., Liu, X., 2019. Direct spectroscopy for probing the critical role of partial covalency in oxygen reduction reaction for cobalt-manganese spinel oxides. Nanomaterials 9, 1–12. https://doi.org/10.3390/nano9040577.
López-Ramón, M.V., Álvarez, M.A., Moreno-Castilla, C., Fontecha-Cámara, M.A., Yebra-Rodríguez, Á., Bailón-García, E., 2018. Effect of calcination temperature of a copper ferrite synthesized by a sol-gel method on its structural characteristics and performance as Fenton catalyst to remove gallic acid from water. J. Colloid Interface Sci. 511, 193–202. https://doi.org/10.1016/j.jcis.2017.09.117.
Lv, Y., Li, Z., Yu, Y., Yin, J., Song, K., Yang, B., Yuan, L., Hu, X., 2019. Copper/cobalt-doped $LaMnO_3$ perovskite oxide as a bifunctional catalyst for rechargeable Li-O_2 batteries. J. Alloys Compd. 801, 19–26. https://doi.org/10.1016/j.jallcom.2019.06.114.
Mahata, A., Nair, A.S., Pathak, B., 2019. Recent advancements in Pt-nanostructure-based electrocatalysts for the oxygen reduction reaction. Catal. Sci. Technol. 9, 4835–4863. https://doi.org/10.1039/c9cy00895k.
Mateus, L., Moreno-Castilla, C., López-Ramón, M.V., Cortés, F.B., Álvarez, M.A., Medina, O.E., Franco, C.A., Yebra-Rodríguez, Á., 2021. Physicochemical characteristics of calcined $MnFe_2O_4$ solid nanospheres and their catalytic activity to oxidize para-nitrophenol with peroxymonosulfate and n-C_7 asphaltenes with air. J. Environ. Manag. 281, 111871. https://doi.org/10.1016/j.jenvman.2020.111871.
Matseke, M.S., Zheng, H., Wang, Y., 2020. The ultrasonication boosts the surface properties of $CoFe_2O_4$/C nanoparticles towards ORR in alkaline media. Appl. Surf. Sci. 516, 146105. https://doi.org/10.1016/j.apsusc.2020.146105.
Mattick, V.F., Jin, X., Yang, T., White, R.E., Huang, K., 2018. Unraveling oxygen electrocatalysis mechanisms on a thin-film oxygen-deficient perovskite $La_{0.6}Sr_{0.4}CoO_{3-\delta}$. ACS Appl. Energy Mater. 1, 3937–3946. https://doi.org/10.1021/acsaem.8b00669.
Mattick, V.F., Jin, X., White, R.E., Huang, K., 2019. Understanding the role of carbon in alkaline oxygen electrocatalysis: a case study on $La_{0.6}Sr_{0.4}CoO_{3-\delta}$/Vulcan carbon composite electrocatalyst. Int. J. Hydrogen Energy 44, 2760–2769. https://doi.org/10.1016/j.ijhydene.2018.12.048.
Mefford, J.T., Hardin, W.G., Dai, S., Johnston, K.P., Stevenson, K.J., 2014. Anion charge storage through oxygen intercalation in $LaMnO_3$ perovskite pseudocapacitor electrodes. Nat. Mater. 13, 726–732. https://doi.org/10.1038/nmat4000.
Osgood, H., Devaguptapu, S.V., Xu, H., Cho, J., Wu, G., 2016. Transition metal (Fe, Co, Ni, and Mn) oxides for oxygen reduction and evolution bifunctional catalysts in alkaline media. Nano Today 11, 601–625. https://doi.org/10.1016/j.nantod.2016.09.001.
Pang, Y., Lei, H., 2016. Degradation of p-nitrophenol through microwave-assisted heterogeneous activation of peroxymonosulfate by manganese ferrite. Chem. Eng. J. 287, 585–592. https://doi.org/10.1016/j.cej.2015.11.076.
Poux, T., Napolskiy, F.S., Dintzer, T., Kéranguéven, G., Istomin, S.Y., Tsirlina, G.A., Antipov, E.V., Savinova, E.R., 2012. Dual role of carbon in the catalytic layers of perovskite/carbon composites for the electrocatalytic oxygen reduction reaction. Catal. Today 189, 83–92. https://doi.org/10.1016/j.cattod.2012.04.046.
Rietveld, H.M., 1969. A profile refinement method for nuclear and magnetic structures. J. Appl. Crystallogr. 2, 65–71. https://doi.org/10.1107/S0021889869006558.

Ryabova, A.S., Bonnefont, A., Simonov, P.A., Dintzer, T., Ulhaq-Bouillet, C., Bogdanova, Y.G., Tsirlina, G.A., Savinova, E.R., 2017. Further insights into the role of carbon in manganese oxide/carbon composites in the oxygen reduction reaction in alkaline media. Electrochim. Acta 246, 643–653. https://doi.org/10.1016/j.electacta.2017.06.017.

Samanta, A., Raj, C.R., 2019. A new approach for the synthesis of electrocatalytically active $CoFe_2O_4$ catalyst for oxygen reduction reaction. J. Electroanal. Chem. 847, 113183. https://doi.org/10.1016/j.jelechem.2019.05.065.

Shinagawa, T., Garcia-Esparza, A.T., Takanabe, K., 2015. Insight on Tafel slopes from a microkinetic analysis of aqueous electrocatalysis for energy conversion. Sci. Rep. 5, 13801. https://doi.org/10.1038/srep13801.

Silva, V.D., Ferreira, L.S., Simões, T.A., Medeiros, E.S., Macedo, D.A., 2019. 1D hollow MFe_2O_4 (M = Cu, Co, Ni) fibers by solution blow spinning for oxygen evolution reaction. J. Colloid Interface Sci. 540, 59–65. https://doi.org/10.1016/j.jcis.2019.01.003.

Stoerzinger, K.A., Risch, M., Han, B., Shao-Horn, Y., 2015. Recent insights into manganese oxides in catalyzing oxygen reduction kinetics. ACS Catal. 5, 6021–6031. https://doi.org/10.1021/acscatal.5b01444.

Suntivich, J., Gasteiger, H.A., Yabuuchi, N., Nakanishi, H., Goodenough, J.B., Shao-Horn, Y., 2011. Design principles for oxygen-reduction activity on perovskite oxide catalysts for fuel cells and metal–air batteries. Nat. Chem. 3, 546–550. https://doi.org/10.1038/nchem.1069.

Tang, W., Wu, X., Li, D., Wang, Z., Liu, G., Liu, H., Chen, Y., 2014. Oxalate route for promoting activity of manganese oxide catalysts in total VOCs' oxidation: effect of calcination temperature and preparation method. J. Mater. Chem. A. 2, 2544–2554. https://doi.org/10.1039/C3TA13847J.

Tian, X., Luo, J., Nan, H., Fu, Z., Zeng, J., Liao, S., 2015. Binary transition metal nitrides with enhanced activity and durability for the oxygen reduction reaction. J. Mater. Chem. A. 3, 16801–16809. https://doi.org/10.1039/C5TA04410C.

Wang, Y., Zhao, H., Li, M., Fan, J., Zhao, G., 2014. Magnetic ordered mesoporous copper ferrite as a heterogeneous Fenton catalyst for the degradation of imidacloprid. Appl. Catal. B Environ. 147, 34–545. https://doi.org/10.1016/j.apcatb.2013.09.017.

Wei, C., Feng, Z., Scherer, G.G., Barber, J., Shao-Horn, Y., Xu, Z.J., 2017. Cations in octahedral sites: a descriptor for oxygen electrocatalysis on transition-metal spinels. Adv. Mater. 29, 1–8. https://doi.org/10.1002/adma.201606800.

Wei, L., Ang, E.H., Yang, Y., Qin, Y., Zhang, Y., Ye, M., Liu, Q., Li, C.C., 2020. Recent advances of transition metal based bifunctional electrocatalysts for rechargeable zinc-air batteries. J. Power Sources 477, 228696. https://doi.org/10.1016/j.jpowsour.2020.228696.

Wu, X., Niu, Y., Feng, B., Yu, Y., Huang, X., Zhong, C., Hu, W., Li, C.M., 2018. Mesoporous hollow nitrogen-doped carbon nanospheres with embedded $MnFe_2O_4$/Fe hybrid nanoparticles as efficient bifunctional oxygen electrocatalysts in alkaline media. ACS Appl. Mater. Interfaces 10, 20440–20447. https://doi.org/10.1021/acsami.8b04012.

Yang, S., Guo, Y., Yan, N., Wu, D., He, H., Qu, Z., Jia, J., 2011. Elemental mercury capture from flue gas by magnetic Mn–Fe spinel: effect of chemical heterogeneity. Ind. Eng. Chem. Res. 50, 9650–9656. https://doi.org/10.1021/ie2009873.

Young, R.A., Mackie, P.E., von Dreele, R.B., 1977. Application of the pattern-fitting structure-refinement method of X-ray powder diffractometer patterns. J. Appl. Crystallogr. 10, 262–269. https://doi.org/10.1107/S0021889877013466.

Zadick, A., Dubau, L., Sergent, N., Berthomé, G., Chatenet, M., 2015. Huge instability of Pt/C catalysts in alkaline medium. ACS Catal. 5, 4819–4824. https://doi.org/10.1021/acscatal.5b01037.

Zhao, Y., Liu, T., Shi, Q., Yang, Q., Li, C., Zhang, D., Zhang, C., 2018. Perovskite oxides $La_{0.4}Sr_{0.6}Co_xMn_{1-x}O_3$ (x = 0, 0.2, 0.4) as an effective electrocatalyst for lithium—air batteries. Green Energy Environ. 3, 78–85. https://doi.org/10.1016/j.gee.2017.12.001.

Zhang, Z., Li, X., Zhong, C., Zhao, N., Deng, Y., Han, X., Hu, W., 2020. Spontaneous synthesis of silver-nanoparticle-decorated transition-metal hydroxides for enhanced oxygen evolution reaction. Angew. Chem. 132, 7312–7317. https://doi.org/10.1002/ange.202001703.

Zhang, Y.-C., Ullah, S., Zhang, R., Pan, L., Zhang, X., Zou, J.-J., 2020. Manipulating electronic delocalization of Mn_3O_4 by manganese defects for oxygen reduction reaction. Appl. Catal. B Environ. 277, 119247. https://doi.org/10.1016/j.apcatb.2020.119247.

Zhou, Y., Xi, S., Wang, J., Sun, S., Wei, C., Feng, Z., Du, Y., Xu, Z.J., 2018. Revealing the dominant chemistry for oxygen reduction reaction on small oxide nanoparticles. ACS Catal. 8, 673–677. https://doi.org/10.1021/acscatal.7b03864.

Zhu, H., Zhang, S., Huang, Y.X., Wu, L., Sun, S., 2013. Monodisperse $M_xFe_{3-x}O_4$ (M = Fe, Cu, Co, Mn) nanoparticles and their electrocatalysis for oxygen reduction reaction. Nano Lett. 13, 2947–2951. https://doi.org/10.1021/nl401325u.